MUSTANG-2 90GHz Observations of Star-Forming Regions From the Star Formation in Radio Survey

Abigail R. Harden,[1] Eric J. Murphy,[2] Eric Faustino Jiménez-Andrade,[2] and Brian S. Mason[2]

[1]*Department of Physics & Astronomy, Agnes Scott College, Decatur, GA 30030, USA*
[2]*National Radio Astronomy Observatory, 520 Edgemont Road, Charlottesville, VA 22903, USA*

ABSTRACT

We present imaging and photometry of 42 nuclear and extranuclear star forming regions in 17 nearby galaxies taken with the Green Bank Telescope (GBT) as part of the Star Formation in Radio Survey (SFRS). Additionally, we used 3, 15, and 33GHz archival VLA data, to probe the radio spectral shape of these regions on ∼1 kpc scales. We found the average spectral index from 3-33 GHz to be -0.25 ± 0.08 with a median absolute deviation of 0.16, and from 33-90 GHz to be -0.02 ± 0.03 with a median absolute deviation of 0.29. Our value of the 3-33 GHz spectral index deviates significantly from the canonical spectral index for star-forming regions of ~ -0.8. Additionally, the large dispersion of 33-90GHz spectral indices indicates a complex and diverse radio spectral shape at frequencies ≥ 33 GHz. Our results demonstrating the need for high-frequency observations that better trace the radio spectra of galaxies, thus allowing a more robust derivation of star formation rates.

1. INTRODUCTION

Radio continuum is a commonly used tracer of massive star formation, and is typically characterized by a power law ($S_\nu \propto \nu^\alpha$). There are several distinct emission mechanisms that contribute to the total emission in the ∼1-100 GHz regime. Both thermal (free-free) and non-thermal (synchrotron) emission are associated with high mass stars ($\geq 8 M_\odot$), which have lifetimes ≤ 10Myr and thus are vital tools for determining the star formation rate (SFR). The strength of thermal emission from HII regions around O and B stars is proportional to the number of ionizing (ie., Lymann continuum) photons from these stars, making thermal emission a reliable and dust free SFR diagnostic (Murphy et al. 2012). These same massive stars end their lives as core-collapse supernovae, whose remnants are the primary accelerator of the cosmic rays (CR) that produce the observed synchrotron emission (Condon 1992). Synchrotron emission dominates the total emission at frequencies less than ∼30 GHz, and has a steep spectral index ($\alpha^{\rm NT} \sim -0.8$) (Murphy et al. 2011). Thermal emission becomes the dominate emission mechanism at frequencies greater than 30 GHz, and typically has a shallower spectral index ($\alpha^{\rm T} \sim -0.1$). Thus radio observations are a useful, extinction free, SFR diagnostic.

aharden@agnesscott.edu

Unfortunately, recent observations have shown that the shape of the radio SED is often more complex than this, and cannot be fully described with just a simple two-component power law. One complicating factor is the presence of anomalous microwave emission (AME), which is possibly rotational emission from dust grains, that causes a excess of emission between ∼10-90 GHz (Linden et al. 2020).

This project is a continuation of the Star Formation in Radio Survey (SFRS; Murphy et al. 2012, 2018; Linden et al. 2020). Linden et al. (2020) used 3, 15, and 33 GHz VLA images to find spectral indices at ∼0.5 kpc scales. With the new Green Bank Telescope (GBT) observations we can put more robust constraints on the non-thermal component of the radio spectra of star forming regions.

Recent observations have shown that the SEDs of many star-forming regions are inconsistent with the canonical values of $\alpha^{\rm NT}$ and $\alpha^{\rm T}$ (eg., Linden et al. 2020; Tabatabaei et al. 2017; Murphy et al. 2011). Thus the primary motivation of the SFRS is to characterize the radio spectra of a large number of nearby galaxies, in order to better calibrate SFR indicators.

This report is organized as follows: In Section 2 we describe the GBT and VLA images used, as well as the analysis procedures. Our results are presented in Section 3 and our conclusions are given in Section 4.

2. DATA AND PHOTOMETRY

We present 90 GHz images of 17 galaxies taken with MUSTANG-2 on the GBT at a resolution of 10". We also used primary-beam corrected VLA images at 3, 15, and 33GHz at a resolution of 2" (Linden et al. 2020). We convolved the VLA images to the same resolution as the corresponding GBT image using the CASA task IMSMOOTH. The source locations are those identified at a 7" resolution by Linden et al. (2020). For all sources we used apertures 2×FWHM of the GBT primary beam, and the median aperture diameter is 1.25 ± 0.5kpc with a median absolute deviation of 0.3kpc.

For sources with only one SF region, the local background was measured in an annulus of width equal to the FWHM at a distance $1.5 \times$ FWHM from the center, as shown in Figure 4. For images with multiple sources, with the exception of NGC 6946 Enuc. 4 and NGC 6946 Enuc. 7 & 9, we used a single annulus that encompassed all of the sources.

3. RESULTS

To characterize the basic shape of the SEDs, we preformed a non-linear least squares fit to the data with a single power law from 3-33GHz and 33-90GHz. The median spectral index from 3-33GHz and 33-90GHz are -0.25 ± 0.08 and -0.02 ± 0.03, respectively. We excluded sources not significantly detected (ie., S/N > 3) in at least two radio bands. Figure 1 shows the distribution of spectral indices for the 42 star-forming regions detected in at least two radio bands. In the 3-33 GHz range, five sources have a rising radio spectra, whereas in the 33-90 GHz regime there are 13 decreasing sources.

To further illustrate the diversity of radio spectra we find, we show NGC 2798 and NGC 2841 as examples. NGC 2798 (Figure 2) has a standard spectra (Figure 3) that is consistent with the typically assumed values of the thermal and non-thermal spectral indices. In contrast, NGC 2841 (Figure 4) has a much more complex spectra (Figure 5).

4. CONCLUSIONS

We have presented 90GHz GBT images of 42 nuclear and extranuclear star-forming regions in the SFRS. We then combined this with 3, 15, and 33GHz images to measure the low (3-33GHz) and high (33-90GHz) frequency spectral indices on ∼1kpc scales.

We find a median spectral index from 3-33GHz of -0.25 ± 0.08 at ∼1kpc scales. This is comparable to the 3-33GHz spectral index of -0.23 ± 0.02 at ∼100pc scales (Linden et al. 2020).

Our results show that the typical two-component power law overly simplifies a galaxies "true" spectra, and thus assuming the canonical value of α^{NT} when calculating the SFR could lead to biases. We found that
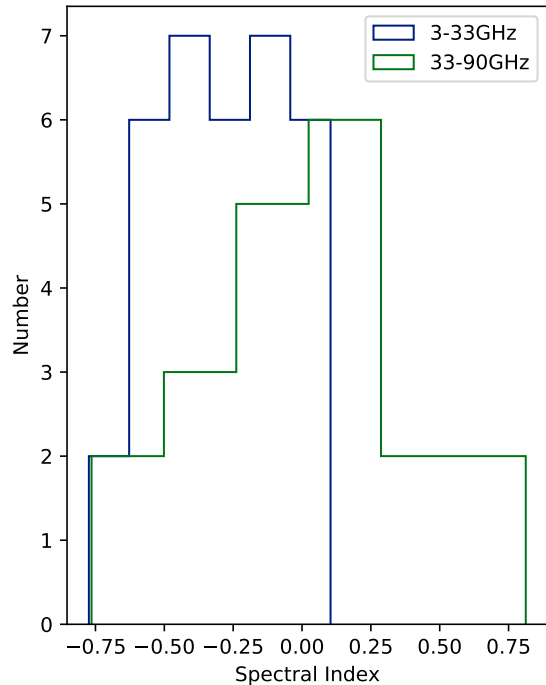
Figure 1. Distribution of the 3-33GHz (blue) and 33-90GHz (green) spectral index for 42 regions.
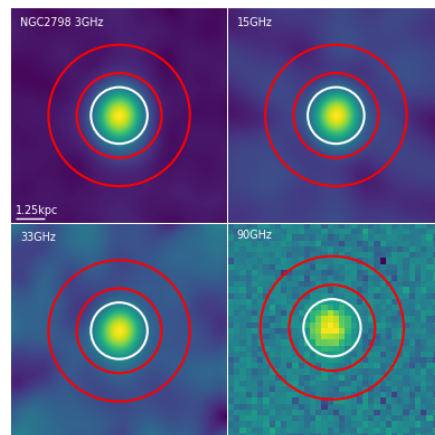
Figure 2. NGC 2798 at 3 (upper left), 15(upper right), 33 (lower left), and 90 GHz (lower right). A scale bar of 10" is given in the lower left corner of the 3GHz image.

most of our sources have a significantly more shallow low-frequency spectral index than the typically assumed value $\alpha^{\mathrm{NT}} \sim -0.8$. Thus assuming this value for standard for standard SFR calculations (eg., Murphy et al. 2017) would overestimate the SFR as compared to what would be found with our measured spectral indices.

Additionally, we found diverse spectral shapes in the $\gtrsim$30GHz regime, including declining, flat, and increasing spectra. These results illustrate the need for more ob-

Table 1. Source Photometry

Source ID	S_{3GHz}	S_{15GHz}	S_{33GHz}	S_{90GHz}	d_{ap}	$\alpha_{3-33\mathrm{GHz}}$	$\alpha_{33-90\mathrm{GHz}}$
	(mJy)	(mJy)	(mJy)	(mJy)	(pc)		
NGC0337a	1.67 ± 0.15	1.31 ± 0.15	<0.65	0.54 ± 0.12	1.78	-0.15 ± 0.08	...
NGC0337b	4.62 ± 0.15	2.6 ± 0.15	1.5 ± 0.23	1.47 ± 0.12	1.78	-0.39 ± 0.06	-0.02 ± 0.04
NGC0337c	0.66 ± 0.15	0.58 ± 0.15	<0.65	<0.35	1.78	-0.09 ± 0.21	...
NGC0337d	0.76 ± 0.15	0.9 ± 0.15	<0.65	<0.35	1.78	0.1 ± 0.18	...
NGC0628a	<0.2	<0.58	<0.25	<0.26	0.79	...	...
NGC0628 Enuc. 1a	1.16 ± 0.09	1.04 ± 0.22	0.48 ± 0.14	<0.28	0.79	-0.3 ± 0.15	...
NGC0628 Enuc. 2a	0.62 ± 0.09	0.31 ± 0.08	0.59 ± 0.17	<0.36	0.79	-0.26 ± 0.27	...
NGC0628 Enuc. 3a	0.76 ± 0.14	0.65 ± 0.15	0.58 ± 0.16	<0.43	0.79	-0.11 ± 0.01	...
NGC0628 Enuc. 4a	0.39 ± 0.09	0.29 ± 0.1	<0.32	<0.45	0.79	...	...
NGC0925a	0.28 ± 0.08	<0.36	<0.25	<0.77	0.95	...	...
NGC2798a	37.01 ± 0.49	12.96 ± 0.23	4.72 ± 0.16	5.04 ± 0.11	2.46	-0.77 ± 0.13	0.07 ± 0.01
NGC2841a	1.9 ± 0.06	1.57 ± 0.09	1.07 ± 0.05	2.12 ± 0.12	1.25	-0.23 ± 0.06	0.68 ± 0.01
NGC3049a	2.99 ± 0.14	1.66 ± 0.14	1.26 ± 0.11	0.74 ± 0.16	2.05	-0.36 ± 0.0	-0.53 ± 0.03
NGC3184a	0.78 ± 0.09	0.42 ± 0.06	0.31 ± 0.05	0.33 ± 0.15	1.05	...	...
NGC3190a	2.57 ± 0.17	0.99 ± 0.25	0.63 ± 0.16	0.42 ± 0.13	1.87	-0.59 ± 0.0	-0.41 ± 0.07
NGC3198a	1.36 ± 0.08	0.76 ± 0.08	0.27 ± 0.09	0.5 ± 0.16	1.23	-0.36 ± 0.05	...
NGC3351a	12.42 ± 0.34	4.69 ± 0.13	3.01 ± 0.22	2.08 ± 0.13	0.96	-0.6 ± 0.01	-0.37 ± 0.02
NGC3351b	12.99 ± 0.34	5.1 ± 0.13	3.3 ± 0.22	1.53 ± 0.13	0.96	-0.58 ± 0.01	-0.76 ± 0.02
NGC3521a	<0.47	<1.22	<0.28	-0.03 ± 0.13	1.0	...	...
NGC3521 Enuc. 1a	<0.38	0.33 ± 0.13	<0.39	<0.47	1.0	...	...
NGC3521 Enuc. 2a	0.91 ± 0.14	<0.51	<0.34	0.47 ± 0.14	1.0	...	...
NGC3521 Enuc. 2b	<0.38	<0.51	<0.34	<0.4	1.0	...	...
NGC3521 Enuc. 3a	<0.35	0.28 ± 0.09	<0.18	<0.54	1.0	...	...
NGC3627a	9.29 ± 0.28	3.6 ± 0.27	2.2 ± 0.22	<2.23	0.94	...	...
NGC3627 Enuc. 1a	3.2 ± 0.22	2.58 ± 0.52	2.04 ± 0.1	<2.71	0.94	...	...
NGC3627 Enuc. 2a	12.48 ± 0.33	6.92 ± 0.69	5.35 ± 0.18	5.95 ± 0.83	0.94	...	...
NGC3773a	2.4 ± 0.06	1.21 ± 0.15	1.07 ± 0.09	0.75 ± 0.16	1.34	-0.36 ± 0.04	-0.35 ± 0.02
NGC3938a	<0.26	<0.12	<0.3	<0.47	1.73	...	...
NGC3938b	<0.26	<0.12	<0.3	<0.47	1.73	...	...
NGC3938 Enuc. 2a	<0.25	<0.19	<0.38	<0.65	1.73	...	...
NGC3938 Enuc. 2b	0.39 ± 0.09	0.31 ± 0.07	<0.38	<0.65	1.73	...	...
NGC6946a	1.08 ± 0.26	1.33 ± 0.18	1.18 ± 0.37	1.35 ± 0.12	0.63	0.07 ± 0.08	0.13 ± 0.09
NGC6946b	48.84 ± 0.26	21.18 ± 0.18	12.92 ± 0.37	12.16 ± 0.12	0.63	-0.53 ± 0.02	-0.06 ± 0.01
NGC6946c	3.74 ± 0.26	2.84 ± 0.18	1.27 ± 0.37	1.66 ± 0.12	0.63	-0.25 ± 0.15	0.27 ± 0.08
NGC6946 Enuc. 1a	0.79 ± 0.18	0.63 ± 0.07	0.71 ± 0.09	<0.56	0.63	-0.02 ± 0.11	...
NGC6946 Enuc. 2a	<0.63	0.72 ± 0.19	<0.37	0.96 ± 0.21	0.63	...	...
NGC6946 Enuc. 2b	2.17 ± 0.23	2.22 ± 0.19	1.83 ± 0.13	1.75 ± 0.21	0.63	-0.07 ± 0.06	-0.04 ± 0.02
NGC6946 Enuc. 3a	<0.5	0.49 ± 0.08	0.33 ± 0.08	0.33 ± 0.21	0.63	-0.52 ± 0.06	...
NGC6946 Enuc. 3b	0.59 ± 0.18	0.79 ± 0.08	0.64 ± 0.08	0.74 ± 0.21	0.63	-0.01 ± 0.17	0.15 ± 0.04
NGC6946 Enuc. 4a	1.93 ± 0.19	2.0 ± 0.08	1.99 ± 0.09	1.76 ± 0.24	0.63	0.01 ± 0.01	-0.12 ± 0.01
NGC6946 Enuc. 4b	<0.49	1.31 ± 0.08	0.73 ± 0.09	1.66 ± 0.24	0.63	-0.74 ± 0.02	0.81 ± 0.04
NGC6946 Enuc. 4c	2.54 ± 0.19	2.16 ± 0.08	1.45 ± 0.09	2.46 ± 0.24	0.63	-0.21 ± 0.13	0.53 ± 0.02
NGC6946 Enuc. 5a	<0.35	<0.21	<0.2	<0.58	0.63	...	...
NGC6946 Enuc. 5b	0.42 ± 0.13	0.47 ± 0.08	0.43 ± 0.07	0.5 ± 0.21	0.63	0.0 ± 0.05	...
NGC6946 Enuc. 6a	2.15 ± 0.25	1.01 ± 0.27	1.53 ± 0.18	1.75 ± 0.18	0.63	-0.17 ± 0.16	0.14 ± 0.03
NGC6946 Enuc. 6b	0.91 ± 0.25	<0.76	<0.51	0.77 ± 0.18	0.63	-0.21 ± 0.25	0.33 ± 0.09
NGC6946 Enuc. 8a	3.41 ± 0.21	1.32 ± 0.1	1.47 ± 0.1	1.28 ± 0.19	0.63	-0.41 ± 0.18	-0.14 ± 0.02

[a]Source locations taken from Linden et al. (2020).
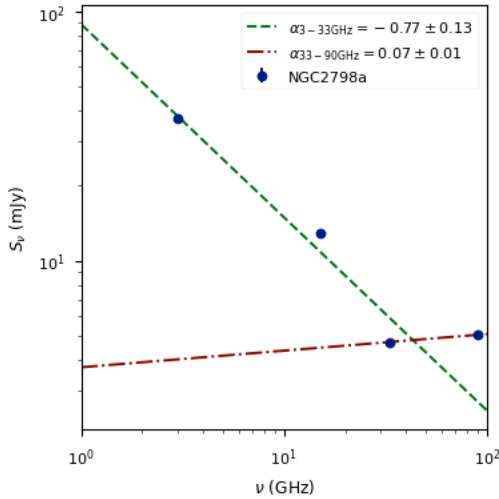
Figure 3. Spectra of NGC 2798 with frequency in GHz on horizontal axis and flux density in Jy on the vertical axis.
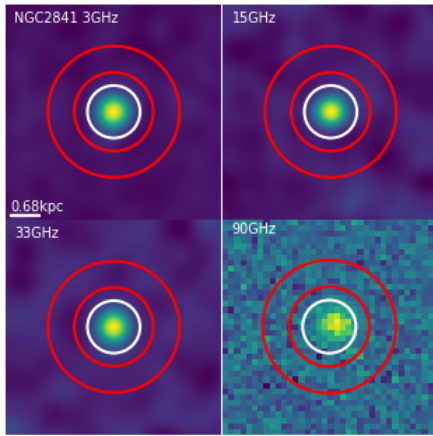
Figure 4. NGC 2841 at 3 (upper left), 15(upper right), 33 (lower left), and 90 GHz (lower right). A scale bar of 10" is given in the lower left corner of the 3GHz image.

servations in the still largely unexplored $\gtrsim$30GHz regime in order to fully characterize radio spectra.

REFERENCES

Condon, J. J. 1992, Annual Review of Astronomy and Astrophysics, 30, 575, doi: 10.1146/annurev.aa.30.090192.003043

Linden, S. T., Murphy, E. J., Dong, D., et al. 2020, ApJS, 248, 25, doi: 10.3847/1538-4365/ab8a4d

Murphy, E. J., Dong, D., Momjian, E., et al. 2018, The Astrophysical Journal Supplement Series, 234, 24, doi: 10.3847/1538-4365/aa99d7

Murphy, E. J., Momjian, E., Condon, J. J., et al. 2017, The Astrophysical Journal, 839, 35, doi: 10.3847/1538-4357/aa62fd

Murphy, E. J., Condon, J. J., Schinnerer, E., et al. 2011, The Astrophysical Journal, 737, 67, doi: 10.1088/0004-637x/737/2/67

Murphy, E. J., Bremseth, J., Mason, B. S., et al. 2012, The Astrophysical Journal, 761, 97, doi: 10.1088/0004-637x/761/2/97

Tabatabaei, F. S., Schinnerer, E., Krause, M., et al. 2017, The Astrophysical Journal, 836, 185, doi: 10.3847/1538-4357/836/2/185
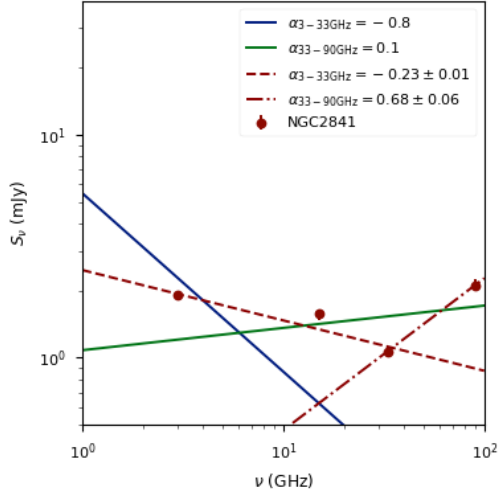
Figure 5. Spectra of NGC 2841 with frequency in GHz on horizontal axis and flux density in Jy on the vertical axis. The red dashed and dot-dashed lines show the low and high frequency spectral index respectively. The blue and green lines represent an "idealized" spectra using the canonical values of $\alpha^{\mathrm{NT}} = -0.8$ and $\alpha^{\mathrm{T}} = -0.1$.